Acta Cryst. (1995). B**51**, 486–501

Crystallography in the Conventional Electron Microscope: Moving Between Direct and Reciprocal Space

BY S. AMELINCKX

EMAT Group, Department of Physics, University of Antwerp (RUCA), Groenenborgerlaan 171, *B*-2020 *Antwerpen, Belgium*

(*Received* 6 *August* 1994; *accepted* 3 *January* 1995)

Abstract

A survey is given of the application of transmission electron microscopy of thin solid films to the study of crystallographic problems. The main feature of electron microscopy is the possibility to observe direct and reciprocal space of the same small crystal fragment and to relate one to the other. This is especially helpful in the study of imperfect structures. Moreover, the local chemical composition can be determined with a fair precision by X-ray microanalysis. The possibility of image defects in diffraction contrast under two-beam conditions, selecting either the direct or the strongly diffracted beam, is due to the spatial variation of the deviation from Bragg's condition along the defects, as a result of local lattice deformation. Such diffraction contrast images are maps of the intensity distribution in the selected diffraction spot; they cannot provide information on the structure. They have been highly successful in the study of the geometry of defects [Head, Humble, Clarebrough, Morton & Forwood (1973), in *Defects in Crystalline Solids*. Amsterdam–London–New York: North-Holland Publishing Co.; Humble (1978), in *Diffraction and Imaging Techniques in Materials Science*, pp. 315–346. Amsterdam–London–New York: North Holland Publishing Co.]. Structural information can be obtained when applying the high-resolution imaging mode, which consists of forming an image by selecting a large number of spots, each spot giving rise to one or several Fourier components contributing to the final image. The images display the configuration of atom columns, in perfect structures as well as round defects. The possibility of imaging atom columns is based on the local nature of electron diffraction. Due to the smallness of the Bragg angles and to multiple diffraction, the electrons are confined to narrow columns on passing through the foil. The atomic columns constitute cylindrically symmetric potential wells which cause channelling of the electrons. By choosing an appropriate set of reflections one can selectively image the structure associated with each sublattice in crystals built on two distinct sublattices, differing sufficiently in unit-cell parameters. In ordered binary alloys selective imaging in the superstructure reflections reveals the sublattice of the minority atom columns. Examples of applications of these different imaging modes are discussed. Electron microscopy has been especially useful in the study of polytypes, intergrowth structures, mixed-layer compounds and long-period structures in general. Several examples of such studies are discussed in some detail, especially in the case of high T_c superconductors. Electron microscopic methods have also been essential in the study of crystals of which only small fragments are available, such as for instance pure fullerenes during the initial stage of this research area. Although convergent-beam electron diffraction is quite useful for a determination of the space group of small crystallites, we have *not* reviewed this method due to space limitations.

1. Introduction

It is the purpose of this paper to show to what extent electron diffraction combined with electron microscopy have become important complementary tools to X- and neutron diffraction in structural studies. *Ab initio* structure determinations by means of electron microscopy are exceptional. However, the structures of stacking variants based on known structures can often be identified on mere inspection of a high-quality high-resolution image. The identification of local variations of the normal stacking has in several cases led to the preparation of new structures in which these deviating stacking modes become the normal ones.

Imaging rather than diffraction will be emphasized since this is specific to electron microscopy. In the same spirit we shall not discuss convergent-beam electron diffraction, which is an important tool in the determination of local symmetry of very small areas. Neither shall we discuss X-ray microanalysis nor EELS (electron energy loss spectrometry), which make chemical characterization possible of the same small crystallite which produced a single-crystal diffraction pattern and an image.

2. Operation modes in electron microscopy

2.1. *Diffraction contrast*

Transmission electron microscopy is essentially a diffraction technique, by means of which imaging is

ISSN 0108-7681

more convenient than with X-rays because of the characteristic features of electron diffraction, in particular the possibility to focus electron beams. The electron wavelength for the commonly used acceleration voltages (>100 kV) is much shorter (10^{-3} nm) than typical interatomic distances in crystals (1 nm) and hence the Bragg angles are quite small and Ewald's sphere can be approximated by a plane. In transmission the electrons propagate through the thin foil specimen along very narrow columns parallel to the incident beam direction (Hirsch, Nicholson, Howie, Pashley & Whelan, 1965). The allowed foil thickness depends on the atomic number of the material and on the accelerating voltage of the microscope; it is normally in the range 10–1000 nm. Electron diffraction is thus a 'local' phenomena, *i.e.* it depends mainly on the local configuration of the scattering centres. The back surface of the foil can be considered as a two-dimensional distribution of point sources of spherical wavelets, of which the amplitudes and phases are determined by the atomic structure in the columns along which the electrons have propagated and have been scattered dynamically. This distribution is periodic for a perfect crystal; deviations from periodicity occur in faulted crystals. The interference of these Huyghens wavelets gives rise to the Bragg diffracted beams, the intensity and positions of which can be recorded as the electron diffraction pattern, *i.e.* as the image of a planar section of reciprocal space. In the electron microscope it is possible to select one or several of these beams by means of an aperture and subsequently magnify the selected diffraction spot by means of a lens system. If a single diffraction spot, either produced by the directly transmitted beam, or by a scattered beam, is selected, one obtains a bright, respectively, dark-field *diffraction contrast image*. Such an image is a map of the intensity distribution in the magnified spot; it does *not* provide information on the crystal structure, but it does reveal defects. Strain fields can be imaged because of the steepness of the rocking curve in the vicinity of the exact Bragg condition, which translates small local orientation differences into significant intensity differences. Also, local differences in magnitude or in the phase of the structure factor can be imaged in this way. Diffraction contrast images are largely independent of the lens aberrations.

2.2. *Lattice fringes*

If by proper positioning of an aperture of a suitable size the direct beam is allowed to interfere with a single scattered beam, a stationary interference pattern is obtained with a period equal to the interplanar spacing of the lattice planes which produce the selected Bragg reflection (Menter, 1956). The crystal plays in a sense the role of a 'beam splitter', similar to Fresnel's biprism producing two interfering beams: the transmitted beam and one dynamically scattered beam. The image of this stationary interference pattern consists of parallel sinusoidal lattice fringes with a period equal to the interplanar spacing; they are in a sense the images of the reflecting planes, *i.e.* of direct space. However, the positions of these fringes depend not only on the specimen but also on the lens aberrations, as well as the imaging conditions. These fringes image the Fourier transform of the selected part of the diffraction pattern, which in this case consists of two beams only. The lattice fringes are well resolved if their separation is within the resolution limit of the microscope. The quality of the lenses, especially of the objective lens, now becomes crucial.

2.3. *Basic principles of structure imaging*

2.3.1. *Image waves model.* In present day microscopes the point resolution routinely achieved is 1.6 Å at 300 kV and 1.0 Å at 1250 kV. In most crystals it is thus possible to image several interplanar spacings even in crystals with small unit cells, such as elemental metals. In such instruments it becomes meaningful to admit a two-dimensional array of diffraction spots through the aperture and image the resulting interference pattern. A microscope with an ideal lens system would then perform the same type of Fourier synthesis as in X-ray diffraction, the phase problem being automatically taken care of by the instrument. The image is then the Fourier transform of the selected part of the diffraction pattern. Unfortunately, the magnetic lenses inevitably exhibit spherical aberration which introduces relative phase shifts among the diffracted beams belonging to different Bragg angles, *i.e.* enclosing different angles with the optical axis of the microscope. These phase shifts depend mainly on the spherical aberration constant of the objective lens, which is a characteristic of the instrument, but also on the defocus, a parameter which can be varied by the observer. Optimum visual contrast is usually achieved at the Scherzer (Scherzer, 1949) value of the defocus (Spence, 1981; Van Dyck, 1978).

Images which bear a direct relation to the structure, *i.e.* in which the atom column positions are imaged as bright or dark dots, are obtained only if all relevant beams are reasonably well transferred and interfere with a reasonably correct phase relation. Under these conditions the image formation can be understood as the result of the superposition of sets of lattice fringes or 'image waves', one set corresponding to each pair of selected reflections. Each set of fringes contributes one Fourier component to the image. The higher the order of the reflection, *i.e.* the longer the diffraction vector, the finer the detail represented. However, if the length of the diffraction vector exceeds a limiting value no amplitude is transmitted through the lens system. This limiting value determines the information limit, which is usually less stringent than the point resolution limit. It is clear that the application of this method requires an instrument with an image transfer function which transmits undamped

beams with as large Bragg angles as possible. Computer simulation programs of images are mostly based on this image formation model. They take damping and phase shifts into account.

The image formation in terms of 'image waves' or Fourier components is illustrated by the sequence of images of Fig. 1, which refers to the 15R polytype of SiC viewed along a close-packed direction. The corresponding diffraction pattern is shown in Fig. 2. In Fig. 1(*a*) two successive reflections of the 000*l* row are made to interfere. Only one-dimensional lattice fringes result with a spacing equal to the repeat distance of the five-layered lamellae, *i.e.* $\frac{1}{3}c$. Only a local shift of the lattice fringes reveals the presence of a stacking fault. Admitting more than five consecutive reflections of the 000*l* row, but still excluding the adjacent parallel dense rows of reflections, it can be seen that there are five fringes in the image period, showing that now individual SiC layers are revealed [Fig. 1(*b*)]. Admitting finally a two-dimensional array of reflections produces an image which reveals the 15R stacking sequence *ABC AC*.... [Fig. 1(*c*)] of the atomic columns.

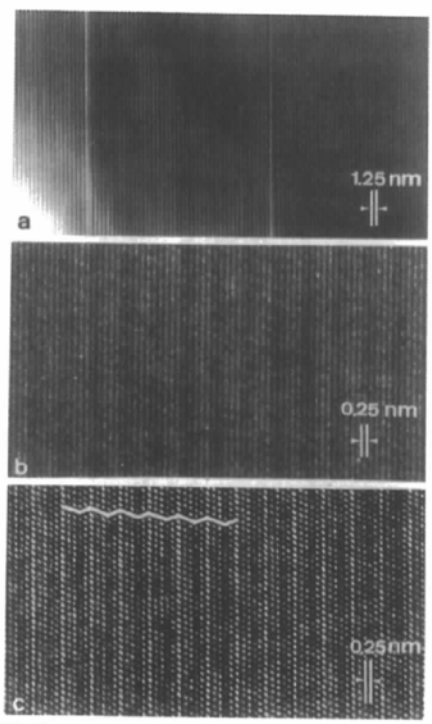

Fig. 1. HREM image formation of the 15R polytype of SiC, as viewed along a closely packed direction: (*a*) two successive spots of the 000*l** row are made to interfere; (*b*) at least five successive spots of the 000*l** reciprocal lattice row are selected; (*c*) several parallel rows of reflections are selected.

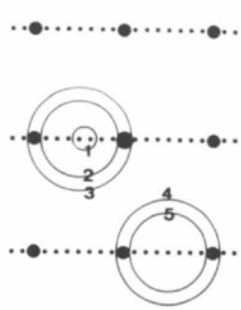

Fig. 2. Schematic representation of the diffraction pattern of the 15R polytype of SiC along the $[11\bar{2}0]^*$ zone. The positions of the selector aperture used to obtain the images of Fig. 1 are indicated.

2.3.2. *Channelling model.* The interaction process with the foil can also be visualized in a quite different manner, emphasizing the local nature of electron diffraction and using the concept of channelling of electrons (Amelinckx & Van Dyck, 1992; Van Dyck, 1990; Van Dyck & Op de Beeck, 1990). It is now assumed that the electrons propagate in the axially symmetric potential well created by a column of atoms parallel to the incident beam. As the electrons move down the column they describe paths which cause alternating periodic focusing and defocusing of the *s*-type electron wavefunctions centred on the columns (Fig. 3). The depth period of this focusing behaviour, which is an extinction distance, depends on the chemical composition of the column and on the separation of the atoms along the column; it decreases with increasing average atomic number per unit length; it is of the order 4–20 nm. Also, the 'phase' of the wavefunction changes on propagating along the column and it changes at a different rate for different columns. As a result, the wavefunction of the imaging electrons at the exit surface of the crystal foil consists of the superposition of the wavefunctions due to the separate columns. For a perfectly periodic crystal this wavefunction has two-dimensional periodicity, but if defects are present it reflects the geometry of the atomic columns at the defect. For this reason high-resolution images can only adequately image defects which can be considered as a two-dimensional configuration of atom columns parallel to the incident beam. This configuration of columns is then represented as a two-dimensional configuration of dots.

2.3.3. *Images as Fourier transforms.* The wavefunction at the back surface of the crystal described either as

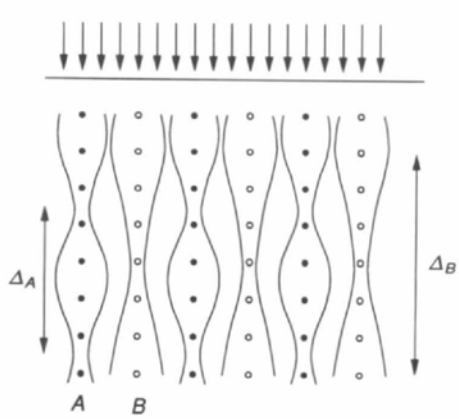

Fig. 3. Periodic focusing and defocusing of the electrons propagating in the cylindrical potential wells associated with atomic columns.

the result of dynamical diffraction or as the result of 'channelling', acts as the periodic object which produces either a diffraction pattern or an image, after magnification and interference (depending on the set of activated lenses), taking into account the angle-dependent phase shifts introduced by the lens system. A column can give rise to either a maximum or a minimum in the centre of the wavefunction, depending on the foil thickness. However, a maximum of the wavefunction is not necessarily imaged as a bright dot, due to the phase shifts introduced by the electron optical lens system.

In mathematical terms one can summarize by stating that the diffraction pattern is the Fourier transform of the object and the image is in turn the inverse Fourier transform of the diffraction pattern. Under ideal conditions, *i.e.* for aberration-free lenses, the Fourier transformation would be completely reversible and the image would be identical to the object. However, the latter transformation is affected by truncation due to the finite apertures and by phase shifts introduced by the lens aberrations. In sufficiently thin foils and for small defocus values, *i.e.* close to the Gaussian focus but different from zero, the image contrast turns out to be proportional to the projected charge density (Lynch & O'Keefe, 1972; O'Keefe, 1973; Lynch, Moodie & O'Keefe, 1973). If the object is a 'weak-phase' object the image contrast is proportional to the projected potential (Cowley, 1950; Cowley & Iijima, 1972; Grinton & Cowley, 1971). In reality, neither one nor the other is strictly applicable.

2.3.4. *Image interpretation.* Since the image details depend on a number of instrumental and observation parameters, as well as on the crystal structure of the object, the interpretation must be carried out with caution. In general, it has to be supported by computer-simulated images based on a postulated model and for a range of different foil thicknesses and focus values. The model is then adjusted until a sufficiently good fit between observed and computed image is achieved at a constant focus, but for the whole range of available thicknesses in a wedge-shaped specimen. In this way the focus, which is not directly measurable, is obtained as well. The required software is available in different versions, which are to some extent all derived from the original multislice procedure of Cowley & Moodie (1957). This interpretation scheme is rather analogous to the trial-and-error method in X-ray structure determination.

Very recently methods have been developed which make it possible to proceed directly from a series of digitized observed images at different closely spaced foci (the focus variation method) to reconstruct the wavefunction in the image plane (phase retrieval). Subsequently, the wavefunction at the exit face of the foil has to be obtained. The final objective is to relate this wavefunction to the structure, which is presented by its lattice potential; this relation depends on the foil thickness. As mentioned above in foils which can to a good approximation be considered as 'weak-phase' gratings, the phase of this wavefunction is proportional to the projected lattice potential. Unfortunately, these conditions are only satisfied in the very thinnest parts of real specimens. If the specimen is thicker but contains well separated atom columns parallel to the incident beam direction, a one-to-one correspondence still exists between extrema of the wavefunction and atom columns. In that case, the relation between wavefunction and structure can be obtained from the channelling theory (Van Dyck *et al.*, 1989).

In practice the desired structural information can often be obtained by visually comparing the observed image with the projection of a structure model obtained from X-ray results. For instance, in studies of homologous series of compounds an 'imaging code' can be established by comparing an image of one of the simple members of the series with the established structure. This often allows the identification of the atom columns associated with certain dot arrays. Symmetry and interatomic distance considerations are of great help in establishing such associations. In this respect it is important to note that due to the imaging procedure the symmetry of an image may be lower than that of the projected atomic arrangement along the imaging zone, but not the reverse. These relations can then be extrapolated to other members of the series and their structures obtained with confidence from images made under similar imaging conditions. This type of method has been applied successfully to the study of polytypes, polytypoids, mixed-layer compounds and intergrowth structures.

Direct *ab initio* structure determinations based exclusively on electron microscopy and electron diffraction are exceptional (Dorset, 1978, 1985). Electron microscopic studies usually make use of *a priori* knowledge obtained by other methods. It is nevertheless especially useful in cases where only powdered specimens of an unknown material are available. In such cases electron diffraction allows one to obtain single-crystal diffraction patterns and hence to determine the lattice parameters unambiguously, albeit with limited accuracy, as well as the diffraction conditions and hence the space group. An X-ray powder diffraction pattern can then easily be indexed and subsequently accurate lattice parameters can be measured and using the Rietveld method the structure refinement can be carried out.

3. Specific imaging modes

3.1. *Selective imaging by beam-selection: binary alloys*

By an adequate choice of imaging conditions it is possible to selectively reveal a subset of atom columns in a structure. For example, in binary-ordered alloys it is often possible to image only the minority atom columns as bright dots (Amelinckx, 1978/1979; Van Tendeloo &

Amelinckx, 1978*a*,*b*). Once the positions of the minority atoms are determined from two projections the complete structure is known.

Superstructures of binary alloys based on the FCC structure exhibit a [100]-zone diffraction pattern consisting of strong FCC spots and weaker superstructure spots, as for instance in Au_4Mn [Fig. 4(*a*)]. The superstructure spots contain information concerning the superstructure, in particular the atom positions are determined by the unit-cell size and shape, and these in turn are determined by the configuration of minority atom columns. The latter can be imaged by collecting the superstructure spots within the circular area centred on the origin, excluding the square of FCC reflections 200, 020, $\bar{2}00$, $0\bar{2}0$. Alternatively, one can exclude the origin and collect all superstructure spots within the square of reflections 000, 200, 020, 220. The first mode is named the bright-field superlattice mode, whereas the second is the dark-field superlattice mode. Using this last mode, the image of Fig. 4(*b*) was obtained, exhibiting Mn columns in Au_4Mn bright dots. Even though a small number of Fourier components (image waves) only contribute to the image, the superstructure is clearly revealed. The positions of the Mn columns with respect to the basic FCC lattice can be deduced from an image made by also including the basic FCC reflections in the aperture. A crystal structure model is compared with the image in Fig. 5. The extra bright dots image the superstructure; they are a subset of a pattern of less bright dots which images the underlying FCC lattice.

The local nature of the imaging process is clearly demonstrated by the possibility to image non-periodic configurations such as [Fig. 4(*b*)]: twin domains and out-of-phase boundaries. This can most readily be understood on the basis of the channelling model, but it is of course also consistent with the image formation model based on 'image waves'.

In areas where twin-related domains based on a common FCC lattice overlap, the lattice of coinciding columns consisting of minority atoms only is imaged as a two-dimensional array of prominently bright dots, illustrating the importance of channelling and the dependence of the dot brightness on the composition of the atom columns (Fig. 6).

3.2. *Selective imaging by shaping the image-transfer function: complex structures*

Selective imaging can also be based on shaping the image-transfer function of the microscope. It allows us to image separately sublattices in complicated structures, provided the average separation of the atom columns on the different sublattices is sufficiently different. The method is based on the fact that the image-transfer function depends among other instrumental parameters, on defocus. It exhibits a main 'window' which transmits a band of spatial frequencies with the correct relative phases, but which quasi-randomly scrambles the phases of the remaining spatial frequencies. As a result, only the sublattice of columns of which the average interatomic distance corresponds with the transmission window will be imaged as sharp dots. By changing the defocus, the position and width of this window can be tuned to a particular band of interatomic distances. The atom columns exhibiting an interatomic distance within this

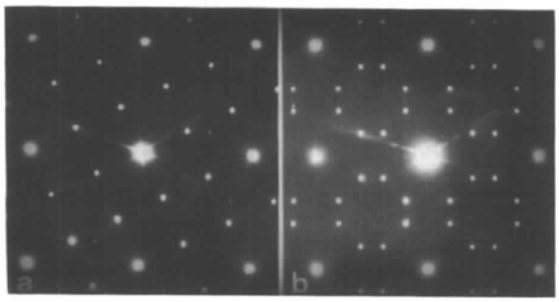

(*a*)

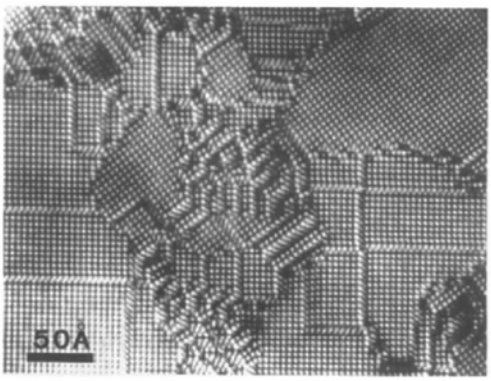

(*b*)

Fig. 4. (*a*) Diffraction pattern of Au_4Mn along [001]. (*b*) High-resolution image of the alloy Au_4Mn obtained using the dark-field superlattice mode. The manganese columns are selectively imaged as bright dots.

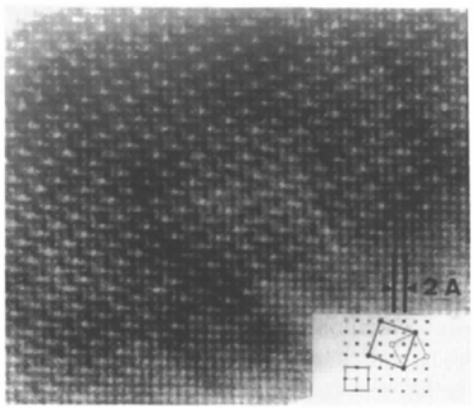

Fig. 5. High-resolution image of Au_4Mn made by also including the reflections of the basic face-centred cubic (FCC) lattice. The manganese columns are imaged as the brightest dots.

band are then revealed as a lattice of bright (or dark) dots. Compounds with compositions in which the abundancies of the different chemical elements are very different are potentially the most suitable objects for the application of this technique, since then also the average distances between chemically similar atom columns are very different for different types of atoms. As an example, we show images of the different sublattices of heavy atoms in $Ba_2NaNb_5O_{15}$ (Fig. 7), in comparison with the structure model (Van Tendeloo, Van Dyck & Amelinckx, 1986).

The narrow secondary windows in the transfer function can under very specific conditions be exploited to image certain simple structures, such as silicon, with a resolution exceeding the point resolution of the microscope (Hashimoto, Endo, Takai, Tomita & Yokota, 1978/1979).

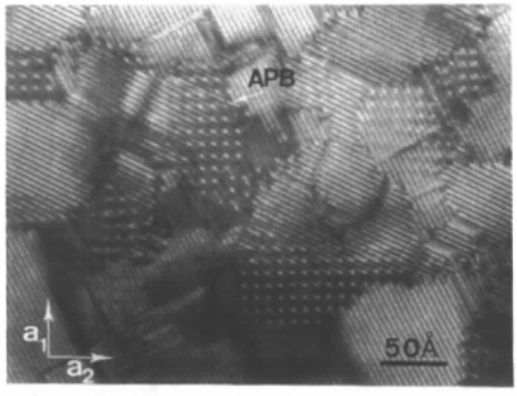

Fig. 6. Image of coincidence site lattice between two overlapping orientation variants of Au_4Mn. The brightest dots image the coincidence columns.

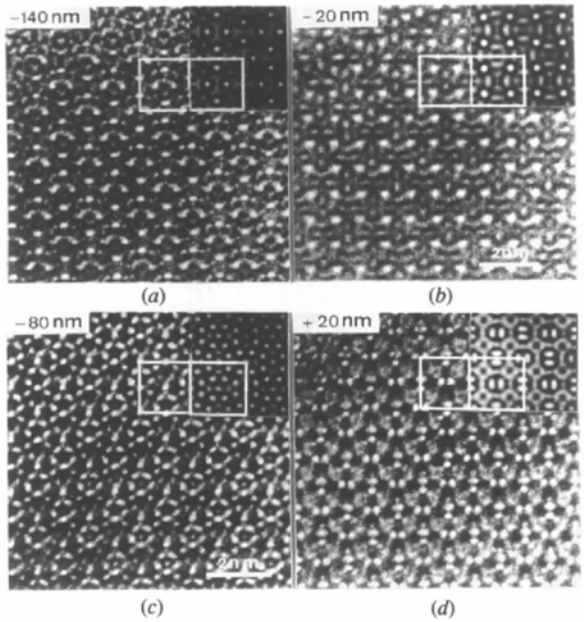

Fig. 7. Selective imaging of different heavy-atom sublattices in $Ba_2NaNb_5O_{15}$: (*a*) at the defocus $\Delta f = -140$ nm the Ba sublattice is imaged; (*b*) at $\Delta f = -20$ nm the Na sublattice is imaged; (*c*) at $\Delta f = -80$ nm the Nb sublattice is imaged; (*d*) at $\Delta f = +20$ nm a complex image is obtained.

3.3. *Selective imaging by reciprocal lattice sectioning: incommensurate intergrowth structures*

A rather specific selective imaging method of a different nature can be applied to intergrowth structures which are based on two different interpenetrating sublattices (Milat, Van Tendeloo & Amelinckx, 1993; Milat, Van Tendeloo, Amelinckx, Babu & Greeves, 1992*a*,*b*; Amelinckx, Milat & Van Tendeloo, 1993). The method is in fact a generalization of that applied to superstructures in binary alloys. In these alloys the basic reciprocal lattice is a sublattice of the superstructure reciprocal lattice. The two lattices differ by the density of nodes since they coincide in part only. In the case of intergrowth structures the two reciprocal lattices are in general spatially separated, except for a small number of common rows or planes. If the angular separation of homologous reciprocal lattice planes is sufficiently large (exceeding 3–4°), one can separately excite a reciprocal lattice section of one or the other substructure and hence image the two substructures separately. By using a common reciprocal lattice section the spatial relation between the two structures can be revealed.

This method was applied to the study of the compounds with incommensurate intergrowth structures $Ca_{0.8}CuO_2$ (Milat, Van Tendeloo, Amelinckx, Babu & Greaves, 1992*a*) and $(Ca,Sr)_{14}Cu_{24}O_{41}$ (Milat, Van Tendeloo, Amelinckx, Babu & Greaves, 1992*b*), which are byproducts of the preparation of high T_c superconductors.

The structural model of $(Ca,Sr)_{14}Cu_{24}O_{41}$ is represented in Fig. 8. The two interpenetrating substructures will be labelled 'sheet' and 'chain' structures. The sheet structure consists of layers parallel to (010), containing zigzag chains along the [001] direction formed by edge-sharing square planar CuO_4 clusters. These zigzag chains are interconnected by bridging O atoms so as to give rise to a planar 'sheet' with composition Cu_2O_3 leaving vacant squares. The Sr/Ca ions occupy the sites, indicated by crosses in Fig. 8(*a*), which project along the [010] direction in the centres at these vacant squares. This substructure is based on an orthorhombic lattice with parameters $a_s = 1.1$, $b_s = 1.29$ and $c_s = 0.391$ nm. The 'chain' structure with composition CuO_2 consists of separated planar chains of edge-sharing CuO_4 clusters, parallel to the [001] direction [Fig. 8(*b*)]. The lattice is face-centred orthorhombic with the same a and b parameters as the sheet structure ($a_c = a_s$; $b_c = b_s$), but with a different c parameter, $c_c = 0.275$ nm. The ratio $c_s/c_c = 2^{1/2}$, and hence incommensurate. The complete structure, which can be described as a succession of layers along the [010] direction

$$\underset{\text{sheet}}{[(Sr,Ca)\text{–}Cu_2O_3\text{–}(Sr,Ca)]}\text{–}\underset{\text{chain}}{[CuO_2]},$$

is represented in Fig. 8(*c*). The corresponding reciprocal lattices as viewed along the common *a** direction are represented in Fig. 9. The large dots represent the reciprocal lattice nodes of the 'sheet' structure, whereas the smaller dots are the nodes due to the 'chain' structure.

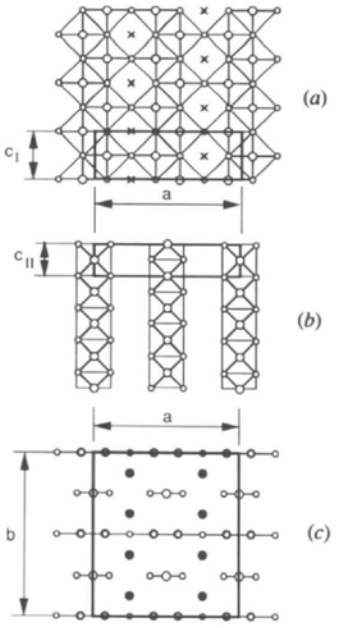

Fig. 8. Structure model of $(CaSr)_{14}Cu_{24}O_{41}$. The structure consists of two interpenetrating substructures: (*a*) the 'sheet' structure with composition Cu_2O_3; (*b*) the 'chain' structure with composition CuO_2; (*c*) the complete structure as viewed along [00*l*].

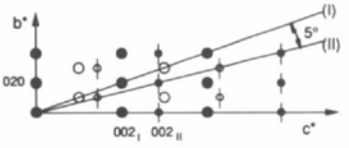

(*a*)

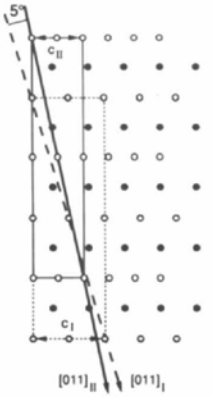

(*b*)

Fig. 9. (*a*) Reciprocal lattice sections I and II of the compound $(CaSr)_{14}Cu_{24}O_{41}$; (*b*) corresponding direct lattice directions.

The two (110)* sections labelled I and II in Fig. 9 differ by *ca* 5° in orientation; they can be used to excite selectively the 'sheet' and the 'chain' reflections.

The diffraction patterns produced by the two sections I and II are shown in Figs. 10(*b*) and (*d*), respectively, and the corresponding images in Figs. 10(*a*) and (*c*). The diffraction pattern of the 'sheet' structure [Fig. 10(*b*)] exhibits sharp spots, whereas that of the 'chain' structure consists of heavily streaked spots [Fig. 10(*d*)]. The images can be compared with the models of Figs. 8(*a*) and (*b*). In Fig. 10(*a*) all heavy atoms of the sheet structure are revealed; the brightest dots correspond to copper columns; the less bright dots to (Sr, Ca) columns. In Fig. 10(*c*) the sharp spots mark the positions of copper columns, whereas the continuous bright lines correspond to rows of vacant space. Figs. 10(*f*) and (*e*) are, respectively, the diffraction pattern and the image produced by the common reciprocal lattice section (010)*. All the heavy atoms columns of the complete structure are now marked by bright dots.

In order to study in particular the spatial relationship between the two substructures over a larger area a rudimentary image was made using the four encircled reflections in Fig. 10(*e*) belonging to the common reciprocal lattice section. This 'low-resolution' image is

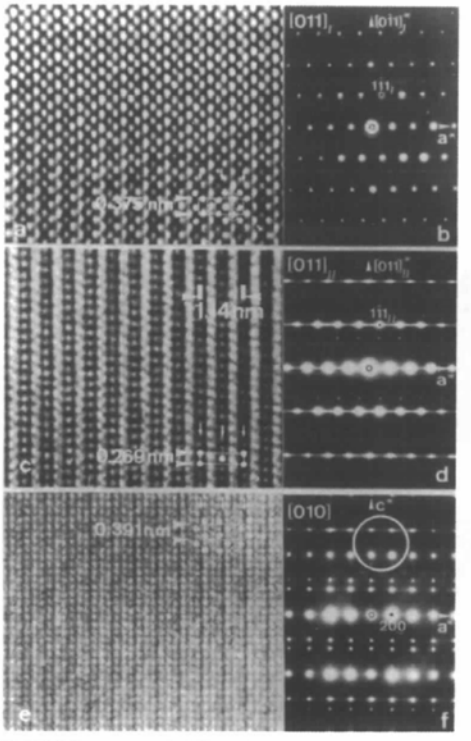

Fig. 10. HREM images and diffraction patterns of $(CaSr)_{14}Cu_{24}O_{41}$: (*a*) HREM of the 'sheet' structure viewed along $[011]_I$; (*b*) diffraction pattern corresponding to (*a*); (*c*) HREM of the 'chain' structure viewed along $[011]_{II}$; (*d*) diffraction pattern corresponding to (*c*); (*e*) HREM of the full structure along the common zone [010]; (*f*) diffraction pattern corresponding to (*e*).

shown in Fig. 11; it reveals a faulted two-dimensional array of bright dots, containing rectangular and parallelogram-shaped meshes. The vertical rows of dots result from the interference between pairs of beams belonging to the same sublattice; these rows are clearly parallel, straight and equidistant. However, the horizontal rows in Fig. 11 are wavy: they are produced by the interference of pairs of beams belonging to different sublattices. This image suggests clearly that the 'chain' and 'sheet' sublattices are shifted relative to each other along the c^* direction over a distance which is variable over the specimen area. The image maps this relative shift. This interpretation is consistent with the streaking observed in Fig. 11(*d*) and which can be attributed to variable relative longitudinal shifts of the 'chains', compared with the rather perfect 'sheet' structure.

Similar observations have been made on the intergrowth structure of $Ca_{0,85}CuO_2$. In this compound the orthorhombic CuO_2 substructure consists of ribbons (or chains) of edge-sharing CuO_4 groups, parallel to $[100]_0$. The Ca ions occupy the octahedral interstices in the rows of oxygen octahedra left between the CuO_4 chains. However, not all such interstices can be occupied resulting in non-stoichiometry (Fig. 12). The Ca ions form a second substructure based on a monoclinic, pseudo-orthorhombic sublattice ($\beta_m = 87°$) with an a parameter $a_{Ca} = 0.33$ against $a_{Cu} = 0.28$ nm, whereas $b_{Ca} = b_{Cu} = 0.63$ and $c_{Ca} \simeq c_{Cu} \simeq 0.6$ nm. Along the a direction six Cu–Cu spacings correspond to five Ca–Ca spacings. This relation is confirmed by the bright dot sequences in the image of the thin part of the specimen, viewed along the common [010] zone (Fig. 13). It is consistent with the macroscopic composition of the compound and it suggests that the Ca ions are roughly equally spaced along the channels formed by the CuO_4 chains, but do not all occupy the centres of octahedra.

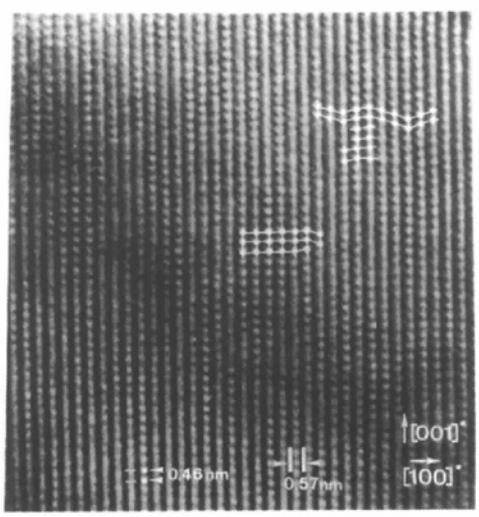

Fig. 11. Image of $(CaSr)_{14}Cu_{24}O_{41}$ along the common [010] zone made in the four reflections encircled in Fig. 10(*f*). The image reveals the relative positions of the two sublattices.

3.4. *Superstructures in layered compounds*

Usually the most informative imaging zones are high-symmetry low-index directions along which the separation of homologous atom columns is largest. However, it is sometimes more relevant to image along a high-index zone. A specific imaging mode can be used for layered structures in which a superstructure occurs in certain layers only. From the diffraction pattern along the zone normal to the layers one can deduce the zone axis along which the separation of the homologous atom columns within the layers will be largest; this zone may be a high-index zone of the basic structure. Imaging along such a zone then often results in the absence of a dotted contrast along most layers, because the column separation is beyond the resolution of the microscope. However, the layers exhibiting the superperiod will then selectively be resolved and revealed by dot sequences. This imaging mode allows in particular to localize the layers responsible for the superstructure; it was, for instance,

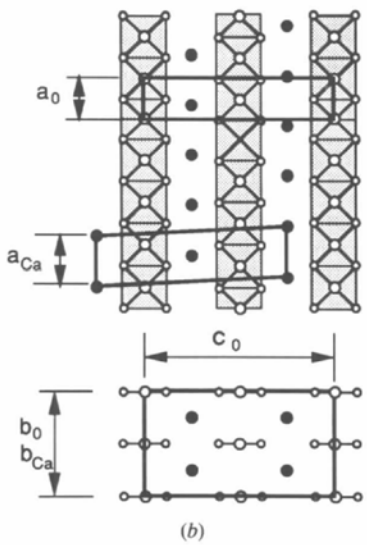

(*b*)

Fig. 12. Schematic representation of the structure of $Ca_{0,85}CuO$: (*a*) viewed along the [010] zone and (*b*) viewed along the [100] zone.

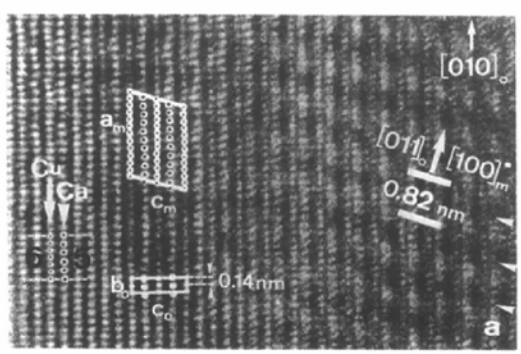

Fig. 13. HREM of $Ca_{0,85}CuO_2$ along the [010] zone. In the thin part (left), six Cu—Cu spacings are seen to correspond to five Ca—Ca spacings.

applied to the study of the superstructure in a cobalt-substituted 1-2-3 compound with the composition $YSr_2Cu_2CoO_{7-\delta}$ (Krekels, Van Tendeloo, Amelinckx, Karpinski, Kaldis *et al.*, 1991; Krekels, Van Tendeloo, Amelinckx, Karpinski, Rusiecki *et al.*, 1991).

4. Examples of electron microscopic studies

4.1. *Long-period alloy structures*

Long-period alloy structures derived from the face-centred structure by the periodic occurrence of antiphase boundaries can be very conveniently studied by a combination of electron diffraction and electron microscopy. The geometry of the diffraction pattern exhibits characteristic features which allow one to deduce a model. Let the long-period structure be formed from the basic FCC structure by introducing a set of parallel out-of-phase boundaries with unit normal $\mathbf{e}_n$, spacing D and displacement vector $\mathbf{R}_0$. In most cases $\mathbf{e}_n = [001]$ and $\mathbf{R}_0$ is of the form $1/2\langle 110\rangle_{FCC}$. The positions of the superstructure spots are given by the following reciprocal lattice vectors $\mathbf{H}$ (Van Landuyt, De Ridder, Gevers & Amelinckx, 1970)

$$\mathbf{H} = \mathbf{h} + (m + \mathbf{h}.\mathbf{R}_0)q\mathbf{e}_n,$$

with $q = 1/D$, $m =$ integer. The spots (*i.e.* satellites) form equally spaced sequences with spacing q and which are shifted with respect to the positions of the basic spots $\mathbf{h}$ over a fraction $\mathbf{h}.\mathbf{R}_0$ of the interspot distance. From the geometrical features of the diffraction pattern, a model for the interface modulated structure can be deduced provided the basic structure is known. The interfaces are normal to the direction of the satellite sequences. Their spacing is the inverse of the satellite spacing and the projection of $\mathbf{R}_0$ on the diffraction vector $\mathbf{h}$ is given by the observed fractional shift $\mathbf{h}.\mathbf{R}_0$. These considerations can readily be generalized to two- and three-dimensional long-period alloys. Imaging the minority atom columns reveals the structure directly. Fig. 14 shows, for instance, the manganese columns in the monoclinic one-dimensional long-period superstructure of the Au_4Mn structure, as viewed along the [010] direction; its ideal composition is $Au_{22}Mn_6$. The corresponding model is shown in Fig. 15 and the diffraction pattern in Fig. 16; note the fractional shifts (Van Tendeloo & Amelinckx, 1978*a*,*b*).

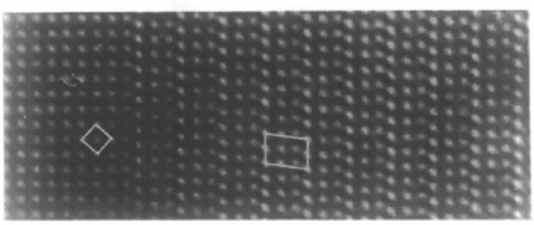

Fig. 14. Monoclinic superstructure of $Au_{4-x}Mn$ with composition $Au_{22}Mn_6$. The bright dots image manganese columns. Non-conservative out-of-phase boundaries occur every third plane.

4.2. *Intergrowth structures*

High-resolution imaging combined with electron and X-ray diffraction has been applied successfully to the study of 'intergrowth' structures. Such structures consist of various sequences of two (or more) different layer-like structural elements which also exist as separate structures when periodically stacked. A condition for the formation of intergrowth structures is the existence of an epitaxial relation between the limiting layers of the two types of lamellae.

A series of intergrowth structures exists for instance in the Ba—Sc—Al—O system (Shpanchenko *et al.*, 1994). The two basic structures $Ba_3Sc_4O_9$ and

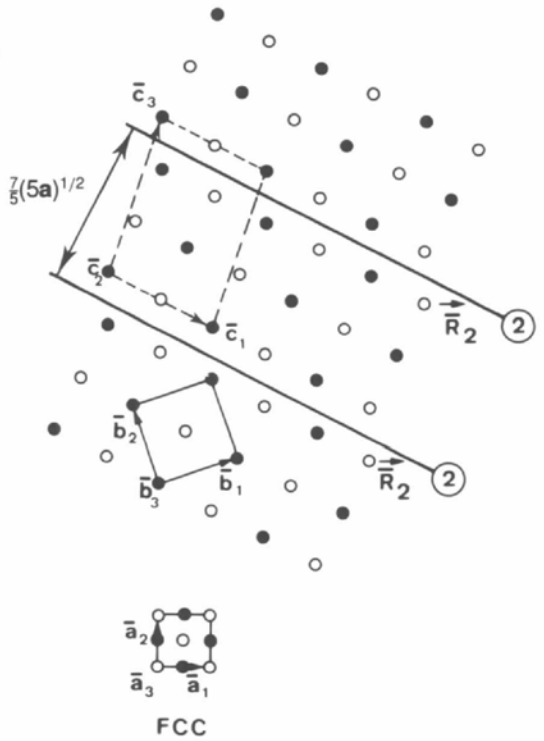

Fig. 15. Model for the structure imaged in Fig. 14. Only manganese columns are shown. The basic structure is face-centred cubic (FCC); the long period structure is derived from the Au_4Mn structure by the introduction of non-conservative antiphase boundaries.

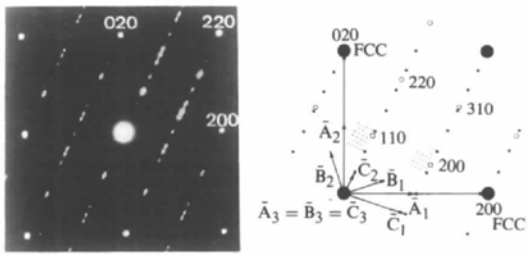

Fig. 16. Diffraction pattern corresponding to the structure shown in Fig. 15 superposed on a diffraction pattern due to Au_4Mn (open dots). The fractional shifts are multiples of 1/5; they are indicated schematically in the right part of the figure.

Ba_2ScAlO_5 are both related to perovskite ABO_{3-x}. Both structures are based on the stacking of close-packed $AO_3(BaO_3)$ layers. In such a layer, a Ba ion is surrounded by six O ions and each O ion by two Ba ions and four O ions. These layers are normally stacked in such a way that the Ba ions in one layer project in the centres of the triangles of Ba ions in the adjacent layers. Between two such layers two types of octahedral interstices occur: mixed interstices, surrounded by Ba and O, and interstices in octahedra formed exclusively by O ions. Only the latter ones are occupied by B cations. Focussing attention on the Ba ions the stacking can be described by the usual symbols ABC ... . The BaO_3 sublattice forms a framework between which B cations are accommodated.

The presence of B cations, represented by Greek letters, adopting a trigonal prismatic configuration may lead to the stabilization of high-energy stacking faults such as $A\beta\gamma A$. Certain layers of cations requiring a tetrahedral configuration can be accommodated by replacing a BaO_3 layer by an oxygen-deficient layer $BaO\square_2$. In this layer a triangle of O ions is replaced by a single O ion located in the centre of the triangle of Ba ions. This results in the formation of two layers of oxygen tetrahedra having their common apices in the oxygen-deficient layer and their parallel triangular bases in the adjacent BaO_3 layers.

The structure of the compound $Ba_3Sc_4O_9$ can be represented by the stacking symbol

$$\ldots|A\gamma B\gamma\alpha B\alpha|C\beta A\beta\gamma A\gamma|B\alpha C\alpha\beta C\beta|\ldots.$$
$$\quad\ \ X\qquad\quad X\qquad\quad X$$

It contains three X-blocks. Emphasizing the chemical composition, the succession of layers in an X-block is

$$\ldots|\ BaO_3\text{–}Sc\text{–}BaO_3\text{–}Sc_2\text{–}BaO_3\text{–}Sc\text{–}BaO_3\ |\ \ldots\ .$$

Note the presence of the vertically stacked pair of A cation layers, *e.g.* $B\gamma\alpha B$. Since there are twice as many B cations per unit area in trigonal prismatic coordination between the two BaO_3 layers as there are cations in pure oxygen octahedral interstices, we write two Greek symbols representing B cations (Sc). The symbol also shows that the occupied trigonal prisms have two different orientations γ and α. The complete structure of $Ba_3Sc_4O_9$ is rhombohedral ($R\bar{3}m$). It is schematically represented in Fig. 17.

The structure X′X′X′, obtained by a 180° rotation of XXX about the c-axis, consists of the same type of lamellae, but it can be distinguished from the XXX structure since a 180° rotation is not a symmetry operation for the structure.

The crystal structure of the second compound Ba_2ScAlO_5 is represented schematically in Fig. 18; its stacking symbol can be written as

$$\ldots|C|\alpha B\gamma A'\gamma B\alpha|C|\beta A\gamma B'\gamma A\beta|C|\ldots. \quad (1)$$
$$\qquad\quad W\qquad\qquad\quad W'$$

It contains two internally twinned lamellae W and W′, related by a 180° rotation about the c axis. The chemical composition of one lamella is given in terms of layers by the succession

$$\ldots|BaO_3|Sc\text{–}BaO_3\text{–}Al\text{–}BaO\square_2\text{–}Al\text{–}BaO_3\text{–}Sc|BaO_3|\ldots\ .$$

The dashed letters in (1) refer to oxygen-deficient BaO layers of the type described above; they are twin planes for the structure, as is evident from the stacking symbol. Aluminium occupies the tetrahedral sites γ alongside these twin planes.

The simplest member of this family of mixed-layer compounds has the structure WXW′X′, where the symbols X, X′, W and W′ represent the lamellae defined above. It has the composition $Ba_7Sc_6Al_2O_{19}$. A high-resolution image made along a zone parallel to the close-packed rows is represented in Fig. 19. The different lamellae can be identified on the basis of geometrical

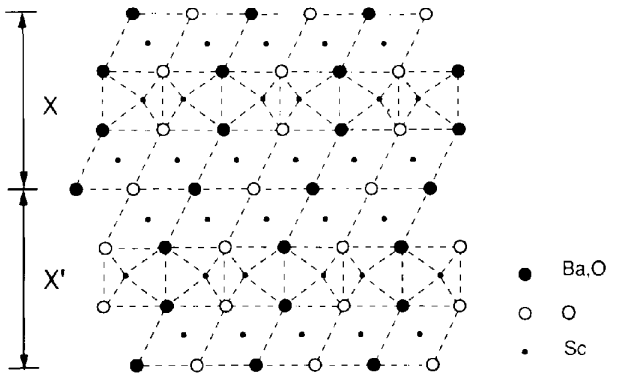

Fig. 17. Schematic representation of the rhombohedral structure of $Ba_3Sc_4O_9$ (XXX...), as viewed along one of the closely packed directions of the (Ba,O) layers. Note the presence of octahedra and of trigonal prisms formed by barium and oxygen.

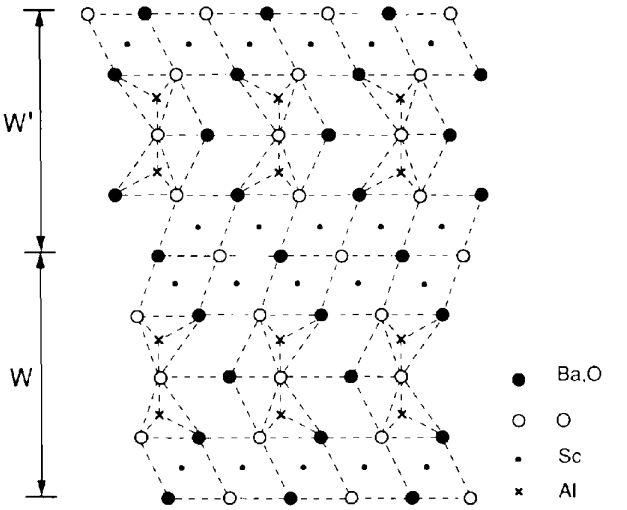

Fig. 18. Schematic representation of the hexagonal structure of Ba_2ScAlO_5 (W′W...) as viewed along one of the closely packed directions of the (Ba,O) layers. Note the presence of octahedra and of tetrahedra consisting of barium and oxygen.

features such as symmetry elements. The singular BaO layers are marked by rows of pronounced bright dots located in the midplanes of the twin lamellae W and W′. The X and X′ lamellae exhibit along their midplanes a line of discontinuity marking the trigonal prismatic layer. This 'vertical' stacking causes a slight discontinuity in the inclined rows of bright dots. These features constitute an 'imaging' code which allows us to identify more complicated sequences on mere inspection of the high-resolution image. It is also possible to identify local stacking sequences which would not be long enough to produce a separate electron-diffraction pattern. Also, singular lamellae in an otherwise periodic sequence can easily be detected.

In the system under discussion next to the basic sequences X X X... and W W′ W W′..., the following periodic sequences were identified:

W X W′ X′; W W′ X W W′ X, W X X W′ X′ X′....

Of course one can envisage many more complicated phases. A simple set of obvious stacking rules has to be satisfied, however. All these phases have different compositions and they are thus composition driven. In principle it is possible to create structures with a predetermined period and sequence of lamellae by a proper choice of the composition. However, the composition differences being small, long heat treatments may be necessary to reach equilibrium and to obtain regular sequences.

4.3. *Defects, domain structures*

Defect studies are often carried out using the diffraction contrast mode, which only reveals the strain field of the defects. Starting from a model derived from image extinctions obtained under two-beam conditions using various diffraction vectors, the strain field can then be determined using a trial-and-error approach. Computer methods are available to perform a detailed analysis of the image profiles due to various types of strain fields (Head, Humble, Clarebrough, Morton & Forwood, 1973; Humble, 1978).

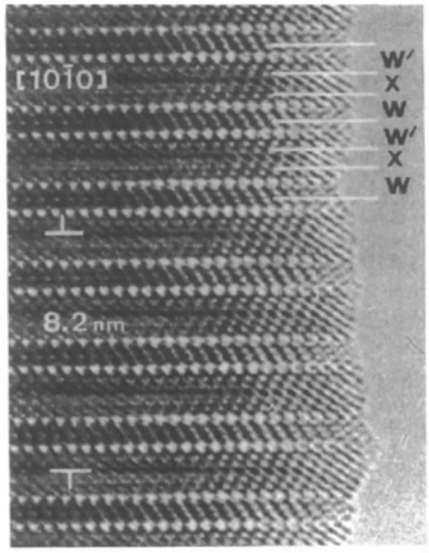

Fig. 19. HREM image along the closely packed rows of atoms in $Ba_7Sc_6Al_2O_{19}$ (W X W′ X′...). The succession of lamellae can be read off on the image. The prominent bright lines represent the mirror planes of W and W′ lamellae. The shift of the atom rows along the central plane of the X-lamellae is visible.

We shall limit ourselves to a few remarks on the use of HREM for line defect studies. Since a high-resolution image is a two-dimensional dot array, each dot imaging an atom column, one can only expect a simple relation between image and line defects if the latter can be considered as a two-dimensional array of straight atom columns parallel to the viewing direction. This condition severely limits the types of defects which can adequately be imaged. The core structures of a number of edge-type dislocations have nevertheless been studied and compared with the predictions of elasticity theory. A projection of the Burgers vector can be found from a Burgers circuit traced on a high-resolution image.

The component, as projected along the viewing direction, of the displacement vector of out-of-phase boundaries and of stacking faults can be deduced directly from the image. Twin boundaries, domain boundaries and grain boundaries in general have been imaged along adequately chosen zones. A major limitation for successful imaging of the latter type of planar defects is the requirement that the viewing direction has to be simultaneously parallel to atom columns in both crystal parts.

4.4. *Molecular crystals*

Since organic molecular crystals are invariably very sensitive to radiation damage by the intense incident electron beams required for imaging, HREM studies have been limited to a few of the most stable molecular crystals, such as for instance the phthalocyanides and more recently the fullerenes. In particular, the structures and microstructures of C_{60} and C_{70} crystals have been imaged and the defects studied on the molecular level. Individual C atoms have not been revealed so far due to the free rotation of the molecules at room temperature, but the stacking of the quasi-spherical molecules and the defects occurring in these crystals have been studied in detail. Due to the small value of the stacking fault energy in van der Waals-bonded crystals, the face-centred cubic crystals of C_{60} exhibit numerous defects of the same type as those occurring in face-centred cubic alloys with a small stacking fault energy: twins, stacking faults, partial dislocations. The image of Fig. 20 shows the microstructure of a C_{60} crystal fragment containing various lattice defects (Muto, Van Tendeloo & Amelinckx, 1993).

Since electron microscopy can be performed on very small single-crystal fragments, the first studies of the crystallography of C_{70} crystals were performed by means

of electron microscopy. These studies led to the discovery of the orientational phase transitions in this material (Van Tendeloo *et al.*, 1992; Verheijen *et al.*, 1992).

Iodine intercalated $C_{60}(I_2)_{2-x}$ was imaged and in particular the rearrangements of the C_{60} molecules accompanying the de-intercalation process were studied in detail (Zhang, Zhang, Amelinckx & Werner, 1994). Also the structure of rubidium-intercalated Rb_4C_{60} could be imaged. In this case, the reactivity of the material made it necessary to prepare the specimen under a protective atmosphere of dry nitrogen and to introduce the specimen into the microscope, keeping the specimen permanently under the same protective gas (Zhang *et al.*, 1994).

4.5. *Recent studies on high T_c superconductors*

High-resolution electron microscopy has been intensively applied to the study of many of the new superconducting phases that appear in the literature almost weekly. Most of these compounds have structures which are closely related to the triperovskite structure and it is therefore often possible to propose a plausible model from the analysis of high-resolution images knowing the composition from X-ray microanalysis; further refinement by the Rietveld method based on X-ray powder patterns is then usually possible.

The 1-2-3 compound $YBa_2Cu_3O_{7-\delta}$ is the archetype of a number of related phases; its structure, as viewed along the [100] zone, together with the corresponding high-resolution image is reproduced in Fig. 21. All heavy-atom columns are imaged; the oxygen columns are not revealed. The succession of layers along the c direction is

$$\ldots\ CuO\text{–}BaO\text{–}CuO_2\text{–}Y\text{–}CuO_2\text{–}BaO\ |\ \ldots\ .$$

The symmetry is orthorhombic pseudo-tetragonal with lattice parameters $a_0 \simeq b_0 \simeq 0.38$ nm; $c_0 \simeq 3a_0$. The loss of tetragonal symmetry is caused by the atomic arrangement in the CuO layers. Along the b_0 direction Cu—O—Cu—O chains are formed. Half the oxygen sites in these layers remain empty; they have to be considered as structural vacancies. Alternatively, one can say that the Cu atoms in these rows are surrounded by O in a square-planar configuration, two O ions belonging to the CuO layer and two to the adjacent BaO layers. Such sequences form chains consisting of rows of corner-sharing CuO_4 groups in planes perpendicular to the a_0 direction.

It was found by means of electron microscopy that specimens of $YBa_2Cu_3O_{7-\delta}$, with $\delta < 0.4$, are invariably twinned on (110) and it was shown by *in situ* observations that the twin fragmentation results from a disorder–order phase transition on the oxygen sublattice in the CuO layers, whereby the symmetry is reduced from tetragonal to orthorhombic and two orientation variants, in which the Cu—O—Cu—O chains are roughly mutually perpendicular, are formed (Zandbergen, Van Tendeloo, Okabe & Amelinckx, 1987; Amelinckx, Van Tendeloo & Van Landuyt, 1989). In the high-temperature tetragonal phase the oxygen is disordered in the CuO layers. On quenching to room temperature from above the transition temperature, the tetragonal phase can be retained as judged from the diffraction pattern, *i.e.* from the absence of twin split spots. However, on a time scale of minutes at room temperature, it is possible to observe *in situ* the formation of a 'tweed' texture, which gradually becomes coarser and finally ends up as a twinned microstructure (Van Tendeloo & Amelinckx, 1987). Close examination of the diffraction pattern shows that already immediately after quenching the spots have the shape of small crosses with arms along [110] and [1$\bar{1}$0]. This demonstrates that the local symmetry is still orthorhombic and that only the macroscopic averaged structure is tetragonal as a result of fine scale twinning. The structure becomes only truly tetragonal for δ close to 1. These experiments also show the high mobility of oxygen in CuO layers, even at room temperature; it is related to the presence of structural vacancies (Van Tendeloo & Amelinckx, 1988).

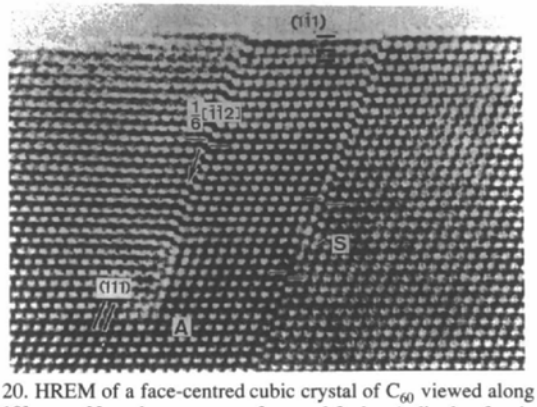

Fig. 20. HREM of a face-centred cubic crystal of C_{60} viewed along the [110] zone. Note the presence of several faults. A dipole of stair-rod dislocations is visible in S. A Frank-type dislocation is visible in A.

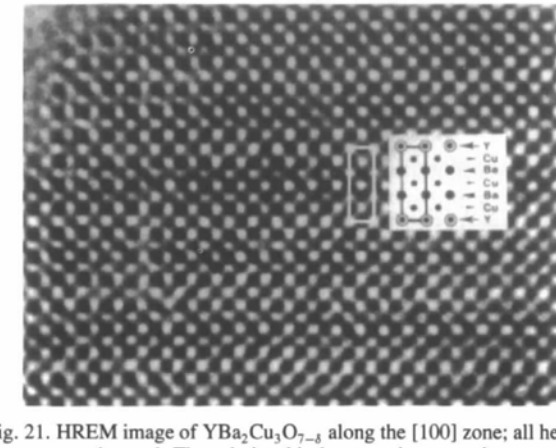

Fig. 21. HREM image of $YBa_2Cu_3O_{7-\delta}$ along the [100] zone; all heavy atoms are imaged. The relationship between image and structure is represented in the inset.

It was furthermore shown that in oxygen-deficient samples ($\delta \approx 0{,}5$) a fraction of the CuO chains may lose all O and become pure Cu rows, in an ordered manner. If every other chain has lost its oxygen the CuO layers contain an alternation of 'filled' and 'empty' chains, leading to doubling of the a_0 parameter. This structure is known in the literature as the $2a_0$ or orthorhombic II structure (Zandbergen, Van Tendeloo, Okabe & Amelinckx, 1987; Reyes-Gasga *et al.*, 1989). Successive CuO layers of this type may stack along c either vertically, keeping the same c_0 parameter, or they may stack in a staggered manner, leading to c parameter doubling. Both arrangements have been observed by imaging and electron diffraction. Often the correlation between the arrangements in successive CuO layers is poor in most samples and extensive streaking along c^* occurs through all superstructure spots. The twinning of the basic structure being present simultaneously with the $2a_0$ structure, two orientation variants of the $2a_0$ structure are usually present giving rise in the diffraction pattern to superstructure spots, suggesting a pattern with fourfold symmetry. In fact, the pattern consists of the superposition of two orthorhombic patterns. The superstructure spots at $h+\frac{1}{2}, k, 0$ are often elongated in the a_0 direction, showing some variability in the spacing between 'filled' (or between 'empty') chains. Occasionally the repeat distance along a_0 is different from $2a_0$, *e.g.* $3a_0$ or fractional, suggesting more complicated sequences of 'empty' and 'filled' chains.

Excess copper is accommodated in the 1-2-3 structure by the formation of double CuO layers instead of single ones. This was first noted by the occurrence of isolated planar defects on (001) planes at the level of the CuO layers (Zandbergen, Gronsky, Wang & Thomas, 1988; Zandbergen, Gronsky & Thomas, 1988). In these double layers the Cu atoms form flat chains of edge-sharing square-planar CuO_4 groups in planes parallel to (100) planes. Their presence causes an offset in the b_0 direction of the crystal parts on both sides of this interface, compared with the normal arrangement. Such a double layer defect viewed along [010] is visible in Fig. 22. This observation suggested the possible stability of structures in which such double layers would occur periodically instead of single CuO layers. It was found that such structures can indeed be prepared, using adequate mixtures of oxides, under normal pressure (Karpinski, Kaldis, Tilek, Rusiecki & Bucher, 1988). Fig. 23(*a*) shows an image of the compound $YBa_2Cu_4O_8$ in which only double chains occur. The rows of elongated bright dots represent the channels between double chains. Electron microscopy has allowed to identify several phases containing periodic arrangements of single CuO layers and double (CuO_2) layers. Fig. 23(*b*) shows for instance an image of the structure of $YBa_2Cu_{3,5}O_{7,5}$ in which single and double CuO layers alternate. The image along the $[010]_0$ zone shows clearly the alternation of single and double layers, whereas this is less obvious along the $[100]_0$ zone, but where now an offset along b_0 can be seen at the double layers (Krekels *et al.*, 1991*a*,*b*).

The structures of the recently discovered mercury-based cuprates (Putilin, Antipov, Ehmaissem & Marezio, 1993) are also of the tetragonal triperovskite type; they are in fact similar to those of the homologous single-layer thallium polytypoids (Verwerft, Van Tendeloo & Amelinckx, 1988; Sleight, Subramanian & Torandi, 1989). The succession of layers along the c direction in the simplest calcium-free compound is

$$\ldots \mid HgO_\delta\text{–}BaO\text{–}CuO_2\text{–}BaO \mid HgO_\delta \ldots .$$

For short it will be designated by the symbol 1201, where the numbers refer successively to the numbers of mercury (thallium), barium (strontium), calcium (yttrium) and copper atoms in the unit cell. The mercury layers are always oxygen-deficient ($\delta < 1, \delta \approx 0.4$). Cu

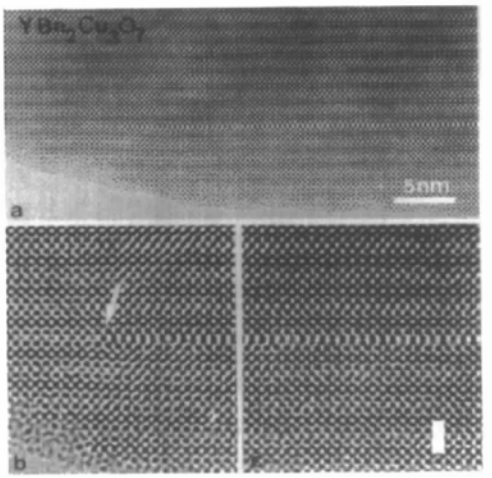

Fig. 22. Double CuO layer in a crystal of $YBa_2Cu_3O_{7-\delta}$ viewed along the [010] zone. (*a*) Small magnification; (*b*) end of the double layer: an edge dislocation is present; (*c*) high magnification of double fault.

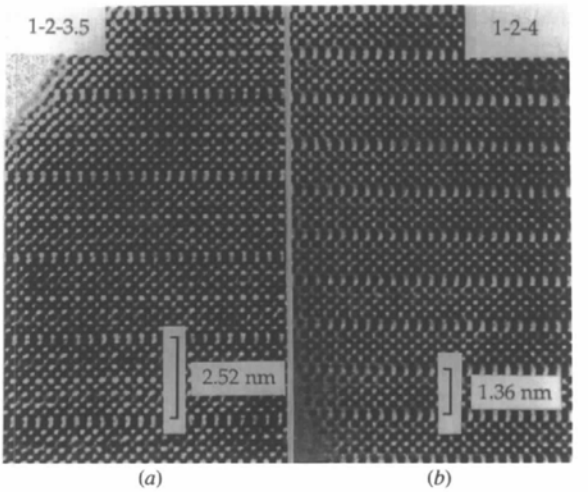

Fig. 23. HREM of the compounds (*a*) $YBa_2Cu_3O_8$ and (*b*) $YBa_2Cu_{3.5}O_{7.5}$ viewed along the [010] zone. The rows of elongated prominently bright dots represent the layers of $(CuO)_2$.

is octahedrally coordinated by O, whereas the BaO and HgO_δ layers are rock-salt-like. Mercury forms a linear arrangement with the apical oxygen ions of CuO_6 octahedra. The structure is represented schematically in Fig. 24. The lattice parameters are $a \simeq a_p = 0.38$ and $c_{1201} = 0.95$ nm.

By Ca(Y) doping it is possible to insert additional copper oxide layers in the unit cell. The succession of layers in the 1212 compound then becomes, for instance

... | HgO_δ–BaO–CuO_2–Ca(Y)–CuO_2–BaO | HgO_δ– ... .

Cu is now fivefold pyramidally coordinated by O. The Ca(Y) layers remain oxygen-free and separate the two CuO_5 pyramids. With increasing Ca(Y) doping, the number of CuO_2 layers also increases; in the 1223 compound the succession of layers is, for instance

...|HgO_δ–BaO–CuO_2–Ca–CuO_2–Ca–CuO_2–BaO|HgO_δ–... .

Structures containing up to seven copper layers have been detected using electron microscopy (Van Tendeloo, Chaillout, Capponi, Marezio & Antipov, 1994; Marezio *et al.*, 1994).

The chemical composition of the members of this homologous series can be summarized by the formula

$$HgBa_2Ca_{n-1}Cu_nO_{2n+2+\delta},$$

or in short, 1, 2, $n-1$, n. It is analogous to the composition of the corresponding homologous series of thallium compounds with the general formula

$$TlBa_2Ca_{n-1}Cu_nO_{2n+3}.$$

The analogy with the Tl compounds suggests that perhaps like in these compounds, also in the mercury-based compounds a second family of phases might occur containing a double HgO_δ layer with a rock-salt structure, leading to a composition 2, 2, $n-1$, n. High-resolution images have in fact occasionally revealed isolated double layers of $(HgO_\delta)_2$, but so far it has not been possible to prepare samples exhibiting systematically double HgO_δ layers. This may be related to the fact that such a double layer can only be stabilized by an oxygen content close to $\delta = 1$.

Samples of the 1201 type with the composition $Hg_xPr_{1-x}Sr_2CuO_{4+\delta}$, where $0.4 < x < 0.5$, exhibit an orthorhombic structure with lattice parameters $a = 0.76 \simeq 2a_p$, $b = 0.368 \simeq a_p$ and $c = 0.888$ nm. This phase is a superstructure of the 1201 structure $HgBa_2CuO_{4+\delta}$ (Goutenoire *et al.*, 1993). By comparing the images along [010] and [100] zones with those of the corresponding praseodymium-free phase it can be concluded that the superperiod must be associated with the arrangement in the mercury-containing layers since these are the only layers exhibiting period doubling, alternating dots having different brightness. The fact that the cations in the other layers exhibit their usual configurations, and the consideration that the only modification in the chemical composition is the addition of praseodymium and the corresponding reduction in mercury content, leads to the assumption that most probably mercury and praseodymium become ordered and give rise to the observed superlattices (Fig. 25). A model in which the mercury rows parallel to the b direction are replaced by the regular alternation of mercury and praseodymium chains parallel to b is consistent with all observations, in particular with the presence of period doubling in the [010] view and its absence in the [100] view. Computer-simulated images based on this model reproduce well the observed images. The model is also consistent with the Hg/Pr ratio. The reason for the preference of Pr for the HgO_δ layers may possibly be understood by noting that the presence of Pr in these layers favours the uptake of oxygen, *i.e.* it causes an increase of δ and hence stabilizes the rock-salt structure of this layer. The ordering is probably a consequence of the difference in ionic radii of Hg^{2+} (0.11 nm) and Pr^{3+} (0.10 nm).

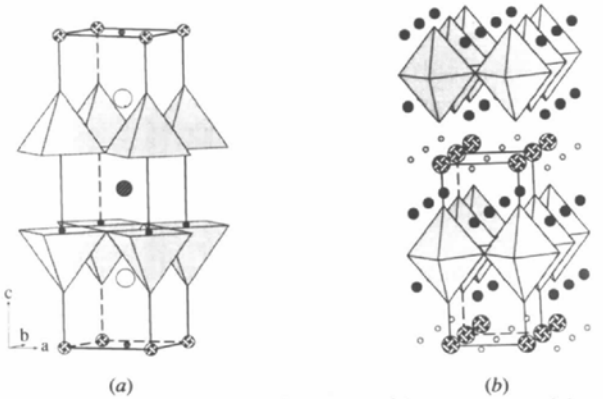

(*a*) (*b*)

Fig. 24. Schematic interpretation of structures of the mercury containing superconductors: (*a*) $HgBa_2CaCu_2O_{6+\delta}$ (1212). The succession of layers from top to bottom is HgO_δ–BaO–CuO_2–(CaY)–CuO_2–BaO–HgO_δ. (*b*) $Hg(BaSr)_2CuO_{4+\delta}$ (1201). The succession of layers from top to bottom in the indicated unit cell is HgO_δ–BaO–CuO_2–BaO–HgO_δ.

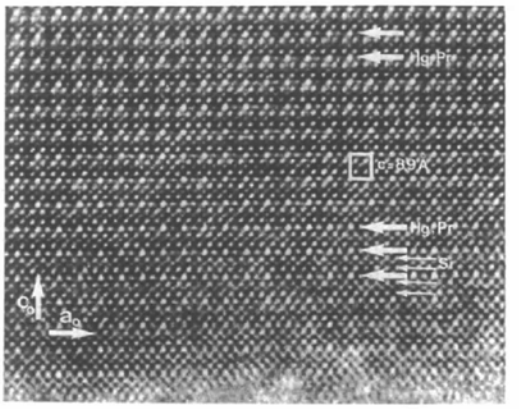

Fig. 25. [010]-zone HREM image of $Hg_xPr_{1-x}(Sr_{2-y}Pr_y)CuO_{4+\delta}$. Note the superperiod at the level of the mercury-containing layers. Alternating bright dots differ slightly in brightness.

The superstructure also causes a slight orthorhombicity of the basic lattice $(a/2)/b = 1.033$. The superstructure clearly allows for coherent twinning on $\{110\}_p$ planes, the rows of Hg and Pr being mutually perpendicular in the two parts of the twin. Such twins have been observed in high-resolution images along the [100] zone. In the diffraction pattern along this zone the presence of twins would simulate fourfold symmetry, provided the orthorhombic deformation of the basic lattice is ignored. However, the latter causes spot splitting of all *hko* spots, except those in the row *hko* perpendicular to the twin interface. This type of boundary has the same geometry as the {110} twins in $YBa_2Cu_3O_{7-\delta}$. However, in the 1-2-3 phase the twins result from the ordering of oxygen and structural vacancies in the CuO layers, forming Cu—O—Cu—O rows parallel to the b_0 directions and no period doubling occurs. The twinning accompanies the tetragonal to orthorhombic phase transition and ensures strain-energy minimization in the orthorhombic phase. In the mercury case alternating chains are assumed to be of a different chemical nature and therefore the *a* parameter is doubled. The twinning perhaps also results from a disorder–order transition between Pr and Hg in preparing the material, the diffusion being facilitated by the oxygen deficiency in the Hg–Pr layers. The orthorhombic deformation of the basic structure is clearly a consequence of the loss of fourfold symmetry in the (Hg–Pr) layers.

4.6. *Static versus dynamic origin of diffuse scattering*

A particularly striking example of the combined use of HREM and electron diffraction pertains to the study of diffuse scattering (Van Tendeloo & Amelinckx, 1986). A simple experiment allows the determination of whether its origin is static or dynamic. A high-quality high-resolution image of the selected area producing the diffuse scattering is Fourier transformed either by making an optical diffraction pattern, using the high-resolution image as a grating, or by computing the transform numerically from a digitized high-resolution image. In case the transform exhibits the same configuration of diffuse intensity as the experimental electron-diffraction pattern, the origin is static. If the transform contains only sharp spots the origin is dynamic. The method is based on the fact that a high-resolution image records the positions of atom columns averaged over a long period (the exposure time of the photograph) compared with the period of any dynamic process involving atom displacements. The interaction time of the electrons with the atoms in the foil in turn is very short compared with the atomic vibration periods. The electrons thus effectively sense a rapid succession of static atom configurations. In the case of scattering by phonons the electron-diffraction pattern results from the superposition of the diffraction patterns produced by these different configurations. Scattered intensity will then be present outside the Bragg spots, even though the average positions of the atom columns remain on the same lattice as in the non-vibrating lattice. The transform then reveals the Bragg spots due to this lattice (Fig. 26). Static displacements locally change the average lattice and hence the transform exhibits diffuse scattering in this case (Fig. 27).

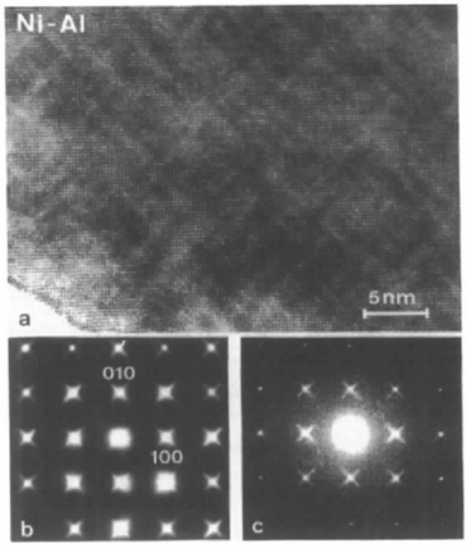

Fig. 26. (*a*) High-resolution image of the 'tweed' structure in NiAl, (*b*) the corresponding electron diffraction pattern and (*c*) the optical diffraction pattern of the HREM image. Note the similarity between (*b*) and (*c*).

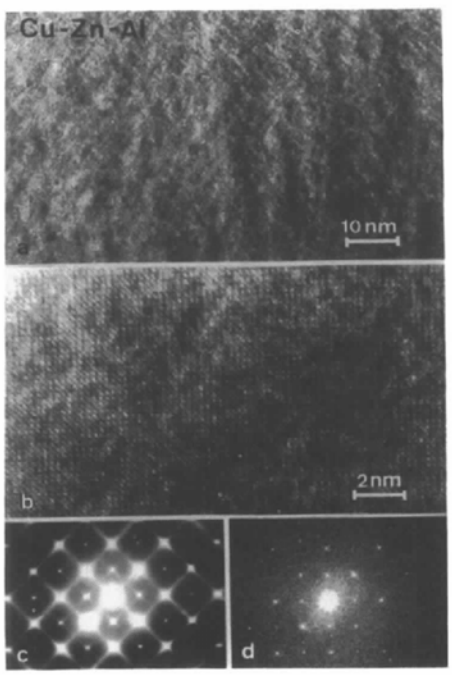

Fig. 27. High-resolution image of the 'tweed' structure in a Cu–Zn–Al alloy in the pre-transition stage: (*a*) low-magnification HREM; (*b*) high-magnification HREM; (*c*) electron diffraction pattern; (*d*) optical diffraction pattern of (*b*). Note the presence of streaks in (*c*) and their absence in (*d*).

Thanks are due to the following colleagues for useful discussions and for their interest: D. Van Dyck, G. Van Tendeloo, J. Van Landuyt, O. Milat and T. Krekels. I am also grateful to G. Van Tendeloo, S. Muto and L. Nistor for the use of photographs from joint papers and of some as yet unpublished photographs.

References

AMELINCKX, S. (1978/1979). *Chim. Scr.* **14**, 197–206.

AMELINCKX, S. & VAN DYCK, D. (1992). In *Electron Diffraction Techniques*, edited by J. M. COWLEY, Vol. 2, pp. 146–154. Oxford Univ. Press.

AMELINCKX, S., MILAT, O. & VAN TENDELOO, G. (1993). *Ultramicroscopy*, **51**, 90–108.

AMELINCKX, S., VAN TENDELOO, G. & VAN LANDUYT, J. (1989). In *Oxygen Disorder Effects in High Tc Superconductors*, edited by J. L. MORAN-LOPEZ & I. K. SCHULLER, pp. 8–18. New York: Plenum Press.

COWLEY, J. M. (1950). *J. Appl. Phys.* **24**, 24–32.

COWLEY, J. M. & IIJIMA, S. (1972). *Z. Naturforsch. Teil A*, **27**, 445–447.

COWLEY, J. M. & MOODIE, A. F. (1957). *Acta Cryst.* **10**, 609–618.

DORSET, D. L. (1978). *Z. Naturforsch. Teil A*, **33**, 964–966.

DORSET, D. L. (1985). *J. Electron Microsc. Tech.* **2**, 89–95.

GOUTENOIRE, F., DANIEL, P., HERVIEU, M., VAN TENDELOO, G., MICHEL, C., MAIGNAN, A. Q. & RAVEAU, B. (1993). *Physica C*, **216**, 243–249.

GRINTON, G. R. & COWLEY, J. M. (1971). *Optik*, **34**, 221–227.

HASHIMOTO, H., ENDO, H., TAKAI, Y., TOMITA, H. & YOKOTA, Y. (1978/1979). *Chim. Scr.* **14**, 23–31.

HEAD, A. K., HUMBLE, D., CLAREBROUGH, C. M., MORTON, A. J. & FORWOOD, C. T. (1973). Computed electron micrographs and defect identification. In series *Defects in Crystalline Solids*, edited by S. AMELINCKX, R. GEVERS & J. NIHOUL. Amsterdam–London–New York: North-Holland Publishing Co.

HIRSCH, P. B., NICHOLSON, R. B., HOWIE, A., PASHLEY, D. W. & WHELAN, M. J. (1965). *Electron Microscopy of Thin Crystals*. Butterworths: London.

HUMBLE, P. (1978). In *Diffraction and Imaging Techniques in Materials Science*, edited by S. AMELINCKX, R. GEVERS & J. VAN LANDUYT, pp. 315–346. Amsterdam–London–New York: North Holland.

KARPINSKI, J., KALDIS, E., TILEK, E., RUSIECKI, S. & BUCHER, B. (1988). *Nature*, **36**, 660–662.

KREKELS, T., VAN TENDELOO, G., AMELINCKX, S., KARPINSKI, J., KALDIS, E. & RUSIECKI, S. (1991). *Appl. Phys. Lett.* **59**, 23–27.

KREKELS, T., VAN TENDELOO, G., AMELINCKX, S., KARPINSKI, J., RUSIECKI, S., KALDIS, E. & JILEK, E. (1991). *Appl. Phys. Lett.* **59**, 23–25.

LYNCH, D. F. & O'KEEFE, M. A. (1972). *Acta Cryst.* A**28**, 536–543.

LYNCH, D. F., MOODIE, A. F. & O'KEEFE, M. A. (1973). *Acta Cryst.* A**29**, 537–535.

MAREZIO, M., ANTIPOV, E. V., CAPONI, J. J., CHAILLOUT, C., LOUREIRO, S., PUTILIN, S. N., SANTARO, A. & THORENCE, J. L. (1994). *Physica B*, **197**, 570–575.

MENTER, J. W. (1956). *Proc. R. Soc. A*, **236**, 119–125.

MILAT, O., KREKELS, T., VAN TENDELOO, G. & AMELINCKX, S. (1993). *J. Phys. J. Fr.* **3**, 1219–1225.

MILAT, O., VAN TENDELOO, G. & AMELINCKX, S. (1992). *Ultramicroscopy*, **41**, 65–85.

MILAT, O., VAN TENDELOO, G., AMELINCKX, S., BABU, T. G. N. & GREAVES, C. (1992*a*). *J. Solid State Chem.* **97**, 405–413.

MILAT, O., VAN TENDELOO, G., AMELINCKX, S., BABU, T. G. N. & GREAVES, C. (1992*b*). *Acta Cryst.* A**48**, 618–624.

MUTO, S., VAN TENDELOO, G. & AMELINCKX, S. (1993). *Philos. Mag. B*, **657**, 513–523.

O'KEEFE, M. A. (1973). *Acta Cryst.* A**29**, 389–396.

PUTILIN, S. N., ANTIPOV, E. V., EHMAISSEM, O. & MAREZIO, M. (1993). *Nature (London)*, **362**, 226–227.

REYES-GASGA, J., KREKELS, T., VAN TENDELOO, G., VAN LANDUYT, J., AMELINCKX, S., BURGGINK, W. H. M. & VERWEIJ, M. (1989). *Physica C*, **159**, 831–852.

SCHERZER, O. (1949). *J. Appl. Phys.* **20**, 20–23.

SHPANCHENKO, R. V., NISTOR, L., VAN TENDELOO, G., AMELINCKX, S., ANTIPOV, E. V. & KOVBA, L. M. (1994). *J. Solid State Chem.* **113**, 193–204.

SLEIGHT, A. W., SUBRAMANIAN, A. & TORANDI, C. C. (1989). *Mat. Res. Soc. Bull.* **14**, 45–52.

SPENCE, J. C. H. (1981). Experimental high resolution electron microscopy. In *Monographs on the Physics and Chemistry of Materials*. Oxford: Oxford Science Publications.

VAN DYCK, D. (1978). In *Diffraction and Imaging Techniques in Materials Science*, edited by S. AMELINCKX, R. GEVERS & J. VAN LANDUYT, p. 355. Amsterdam–London–New York: North Holland Publishing Co.

VAN DYCK, D. (1990). Proc. XIIth Int. Congress on Electron Microscopy, Seattle, USA, Vol. 1, pp. 64–68.

VAN DYCK, D. & OP DE BEECK, M. (1990). Proc. XIIth Int. Congress on Electron Microscopy, Seattle, USA, Vol. 1, pp. 26–30.

VAN DYCK, D., DANCKAERT, J., COENE, W., SELDERSLAGHS, E., BRODDIN, D., VAN LANDUYT, J. & AMELINCKX, S. (1989). In *Computer Simulation of Electron Microscope Diffraction and Images*, edited by W. KRAKOW & M. O'KEEFE, pp. 107–118. Warrendale: The Minerals, Metals and Materials Society.

VAN LANDUYT, J., DE RIDDER, R., GEVERS, R. & AMELINCKX, S. (1970). *Mat. Res. Bull.* **5**, 353–362.

VAN TENDELOO, G. & AMELINCKX, S. (1978*a*). *Phys. Status Solidi A*, **47**, 555–576.

VAN TENDELOO, G. & AMELINCKX, S. (1978*b*). *Phys. Status Solidi A*, **49**, 337–348.

VAN TENDELOO, G. & AMELINCKX, S. (1986). *Scr. Metall.* **20**, 335–356.

VAN TENDELOO, G. & AMELINCKX, S. (1987). *Phys. Status Solidi A*, **103**, K1.

VAN TENDELOO, G. & AMELINCKX, S. (1988). *J. Electron Microsc. Tech.* **8**, 285–297.

VAN TENDELOO, G., AMELINCKX, S., DE BOER, J. L., VAN SMAALEN, S., VERHEIJEN, M. A., MEEKES, M. & MEIJER, G. (1992). *Chem. Phys.* **166**, 287–302.

VAN TENDELOO, G., CHAILLOUT, C., CAPPONI, J. J., MAREZIO, M. & ANTIPOV, E. V. (1994). *Physica C*, **223**, 219–226.

VAN TENDELOO, G., VAN DYCK, D. & AMELINCKX, S. (1986). *Ultramicroscopy*, **19**, 235–247.

VERHEIJEN, M. A., MEEKES, H., MEIJER, G., BENNEMA, P., DE BOER, J. L., VAN SMAALEN, S., VAN TENDELOO, G., AMELINCKX, S., MUTO, S. & VAN LANDUYT, J. (1992). *Chem. Phys.* **166**, 287–302.

VERWERFT, M., VAN TENDELOO, G. & AMELINCKX, S. (1988). *Physica C*, **156**, 607–612.

ZANDBERGEN, H. W., GRONSKY, R. & THOMAS, G. (1988). *Phys. Status Solidi A*, **105**, 207–215.

ZANDBERGEN, H. W., GRONSKY, R., WANG, K. & THOMAS, G. (1988). *Nature*, **331**, 516–518.

ZANDBERGEN, H. W., VAN TENDELOO, G., OKABE, T. & AMELINCKX, S. (1987). *Phys. Status Solidi A*, **103**, 45–60.

ZHANG, X. B., ZHANG, X. F., AMELINCKX, S. & WERNER, H. (1994). *Appl. Phys. A*, **58**, 107–116.

ZHANG, X. B., ZHANG, X. F., BERNAERTS, D., VAN TENDELOO, G., AMELINCKX, S., VAN LANDUYT, J. & WERNER, H. (1994). *Ultramicroscopy*, **55**, 25–30.